Nodule Evolution of Ductile Cast Iron During Solidification

S.C. MURCIA, E.A. OSSA, and D.J. CELENTANO

Ductile cast irons are ferrous alloys in which precipitation of graphite in the form of spherical nodules is embedded in a metal matrix to obtain ductility on the material. Despite the importance of the shape of the nodules, the models proposed to predict the solidification of ductile irons assume a perfect spherical shape during the growing process up to the final solidification of the material, which is proved not to be the case in all castings depending on the processing conditions. The influence of the process parameters on the geometry of the nodules in ductile irons was experimentally evaluated and a model to predict the evolution of nodules during solidification was proposed. The proposed model for growth predicts changes in the nodule count as well as in the nodularity based on different laws for carbon diffusion according to the solid fraction, helping to understand the trends found experimentally.

DOI: 10.1007/s11663-013-9979-5

I. INTRODUCTION

DUCTILE iron (DI) castings are ferrous alloys in which precipitations of graphite are embedded in a metal matrix in the form of spherical nodules. These are industrially used in parts that require moderate ductility without sacrificing mechanical resistance, as in valves, hardware elements, and auto parts. Studies focusing on DI have become important in recent years due to its extensive use and a growing trend to replace forged steels due to their lower comparative costs. Efforts have been made to improve DI mechanical properties by means of alloying, allowing it to replace cast and forged steels in different applications.[1] In order to achieve further improvements in the quality of DI casting parts, it is important to understand the physical mechanisms involved in the solidification process, since its mechanical properties are influenced by the microstructure of the matrix and the morphology of the graphite nodules present.[2–5]

The solidification process of DI begins at high temperatures [~1438 K (~1165 °C)], which makes it difficult to have experimental evidence of the transformation sequence from liquid to solid state. Assuming that the cooling process from the liquid state of a well-inoculated casting occurs under equilibrium conditions (cooling rate ≅ 0), the first solid to precipitate in a hypereutectic DI (carbon equivalent CE = 4.5 pct) is the graphite phase in the form of particles. These graphite particles grow through the depletion of carbon atoms in the liquid iron until the temperature reaches the range of eutectic transformation. Austenite then nucleates in areas of low C concentration; therefore, austenite surrounds graphite nodules. During eutectic solidification, only austenite is in contact with liquid, and carbon diffusion through austenite is the mechanism that controls the nodules' growth.[6–10] After solidification, carbon diffusion continues toward the preexisting graphite nodules since the solubility of carbon in austenite decreases with temperature.[6] Subsequently, eutectoid transformation occurs, where the austenite transforms into pearlite and more carbon atoms diffuse into the nodules. Finally, depending on the amount of carbon (CE), DI metal matrix can be a mixture of ferrite and pearlite.

Some evidence of the solidification process can be found thanks to the microstructures obtained through quenching DI at different temperatures,[7,11,12] giving rise to theories for the solidification process based on different experiments. As a result, various models to predict solidification and nodule growth have been proposed depending on the particular ideas of each researcher and the technical advances achieved through time. Two such models attempt to explain the solidification process of DI with eutectic composition, known as the uninodular[12–16] and multinodular[5,6] theories. The uninodular theory assumes that graphite nodules nucleate in the liquid and are separately surrounded by austenite spherical shells. Both phases grow by means of carbon diffusion from the liquid to the graphite nodules until the end of the solidification (see Figure 1(a)). Some authors argue that although dendritic austenite may be present during the solidification of eutectic composition DIs, it cannot be considered eutectic austenite and should be referred to as "off-eutectic" austenite since it occurs in a composition range different from the eutectic.[5,6,17] From the eutectic phase diagram, it is apparent that a eutectic structure can be obtained only when the composition is exactly eutectic. Nevertheless,

S.C. MURCIA, formerly M.Sc. Student with the Engineering Materials Research Group, School of Engineering, Eafit University, Cra 49 No. 7 Sur 50, Medellín, Colombia, is now Ph.D. Student with the University of Maryland Baltimore, Baltimore, MD. E.A. OSSA, Professor, is with the Engineering Materials Research Group, School of Engineering, Eafit University. Contact e-mail: eossa@eafit.edu.co D.J. CELENTANO, Associate Professor, is with the Mechanical and Metallurgical Engineering Department, Pontificia Universidad Católica de Chile. Vicuña Mackenna # 4860, Macul, Santiago, Chile.

Manuscript submitted June 18, 2013.
Article published online October 26, 2013.

experimental observations show that, depending on the growth conditions, eutectic microstructures can be obtained at off-eutectic compositions.[9] However, this growth form of the graphite is difficult to explain theoretically due to both the time it would take to diffuse the carbon through the austenite as well as the pressures that should be generated in the austenite shell when the sphere of graphite is growing. In order to avoid these issues, the multinodular theory[5,6] proposes that both phases nucleate independently in the liquid. Based on experimental results, this theory considers that austenite grows in a dendritic form and, as solidification proceeds, the dendritic arms surround the graphite nodules[5] [see Figure 1(b)]. A more detailed description of such models can be found in References 5, 13.

One of the main mechanical characteristics of DI is its ductility, which is possible due to the presence of graphite in the form of nodules. This geometry is obtained during its solidification without the possibility of subsequent changes.[18] During the solidification process, the growth of the nodule is restricted due to carbon diffusion through austenite, creating preferential paths of growth, obtaining a shape similar to rose petals as can be seen experimentally (Figure 2). The final shape of the graphite depends mainly on the speed at which austenite envelopes the nodule. This speed depends on the undercooling of the casting, which is also influenced by the amount of magnesium present in the melt.[9] Zhou[11] proposed in 2011 that there are three types of encapsulation of the austenite: fast, slow, or non-existent enveloping. If there is fast enveloping of the nodule, then the graphite would have the same radii for carbon diffusion, which will generate a spherical structure. If there is slow enveloping, the nodule will have preferential areas of growth, decreasing the final nodularity. Lastly, if there is no encapsulation, the final geometry will correspond to laminar graphite.[11]

Although the multinodular theory is based on experimental findings (austenite dendrites in eutectic composition), there have been more studies aimed at simulating the solidification of the DI using the uninodular theory[12–16,19,20] rather than the multinodular theory.[5,6] Additionally, in the existing models, the nucleation and growth of the nodules are expected to create a complete sphere, which is a theoretical and ideal behavior that does not take place in the actual casting process.[21]

The final morphology and count of graphite nodules are studied in this paper. Experimental work was performed in an industrial environment, in order to identify temperature variables that arise from the different production steps that cast iron has to follow before completing its solidification in the foundry floor. A new numerical model was developed for the prediction of nodularity and implemented in an existing multinodular frame. This model allows the comparison with the experimental data and helps to take a further step to understand which thermal variables affect the graphite's shape and count.

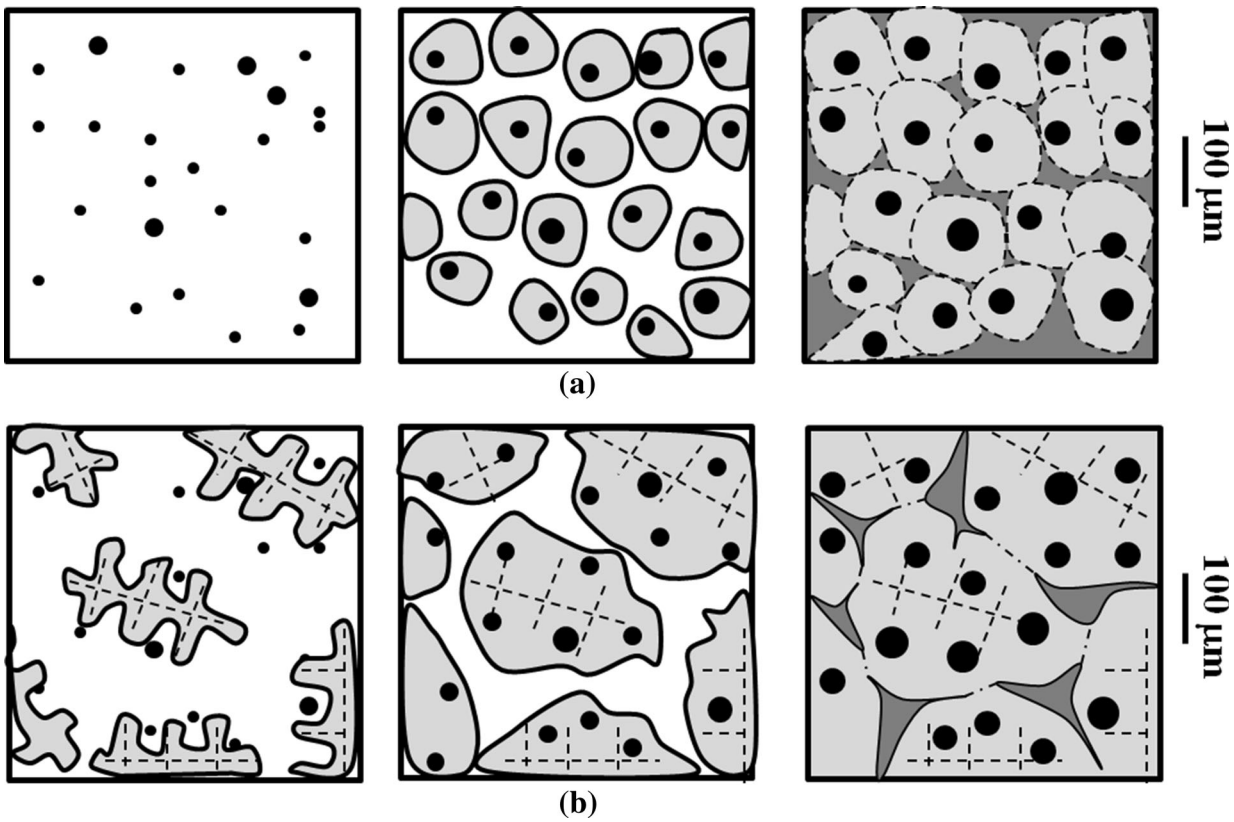

Fig. 1—Microstructural evolution according to the (*a*) uninodular and (*b*) multinodular theories.[7]

II. EXPERIMENTAL PROCEDURE

Three heats of cast iron were prepared in a commercial foundry using an induction furnace with a maximum capacity of 1200 kg, charged with 60 pct of cold-rolled steel and 40 pct of pig iron. Once the materials were melted and the respective carbon and silicon adjusted, the furnace was kept at a temperature of 1823 K (1550 °C). At this point, a sample was taken and chilled for chemical characterization. Since DI has free carbon as graphite, it is necessary to perform rapid cooling of the casting to obtain cementite (Fe_3C) in the majority of the structure.[18] The spheroidizing treatment was performed by means of the sandwich method, where once preheated the ladle, 1.1 pct Fe-Si-Mg, was covered by reaction-retarding material, reducing the Mg evaporation. When the spheroidizing treatment was ended, each melt was divided into 100-kg ladles. A further inoculation was performed in the ladles with 0.3 pct Fe-Si in order to avoid carbide formation. Finally, scum resulting from post-inoculation was removed. The temperature was taken by a pyrometer ElectroNite (thermocouple K) in each step of the production process, *e.g.*, temperature in (i) the oven, (ii) the ladle after the spheroidizing treatment, (iii) the ladle before post-inoculation, and (iv) after scum removal. These temperatures were taken in order to understand the thermal history of the casting before being poured into the sand molds.

In order to evaluate the fading effect of the chemical treatments, time was recorded from the beginning of each process. Using a stopwatch, time was taken from the moment at which the reaction ended for a period of time up to 20 minutes. The melt was poured into step sand molds to study the effect of wall thickness (and therefore cooling rate) on the microstructure of the material, following Kim *et al.*,[22] having wall thicknesses of 10, 30, and 50 mm (see Figure 3). One sand mold per minute was filled, beginning after scum removal until 10 minutes after inoculation. Before pouring the melt, temperature was measured in the ladle. When 10 molds were cast, additional pouring was done at minutes 15 and 20 after the spheroidizing treatment. Additionally, pouring chill samples, which were individually analyzed, captured the evolution of the graphite during this time period.

The average chemical composition of the melts prior to the spheroidizing treatments, obtained by optical emission spectroscopy (OES), is given in Table I. The CE was calculated in order to verify that the melts produced had similar paths during the solidification process. The CE is important since it determines if the DI is hyper, hypo, or eutectic, which modifies the solidification process during eutectic solidification.[18] Taking into account the content of carbon and silicon, the average CE is equal to 4.4 pct, which makes the castings slightly hypereutectic. Since it is close to a eutectic DI, a eutectic model can be used for numerical simulations in the microstructural simulations in the following sections.

Optical microscopy (OM) was used for the microstructural characterization of the castings. Specimens were taken from the last solidification zone of each casting, found by numerical simulation using the software SolidCast® and shown as the highlighted region in Figure 3. As shown in Figure 3, the step mold has two different zones due to the wall thicknesses. The highlighted zone that corresponds to the 50 and 30 mm thickness had a solidification time of 4.71 minutes, while the 10 mm took 1.57 minute to solidify. It is important to emphasize that an area near the edge of the casting mold must be avoided as it might cause an increase in the nodule count due to a higher cooling rate in comparison to the rate to which the entire casting piece was subjected.[23]

Conventional metallographic preparation of the specimens was followed and is described elsewhere.[24] To prevent graphite nodules from tearing from the metal matrix, the polishing procedure was performed manually

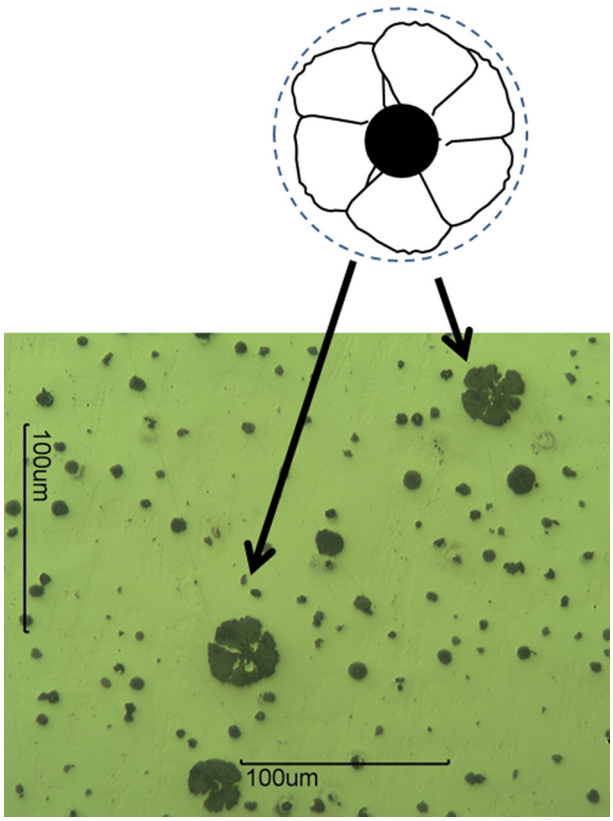

Fig. 2—Nodules' growth as rose petals depending on surrounding austenite.

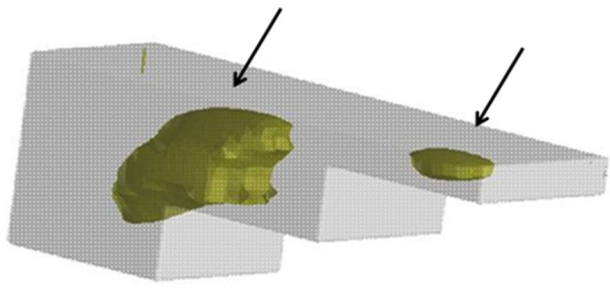

Fig. 3—Sand step mold. The yellowish areas correspond to the last zones to solidify (Color figure online).

using kerosene and wax as a lubricant. Nodule count and nodularity of graphite nodules were analyzed *via* image analysis software. Images were obtained from three sectors of the test piece using a Leitz Metallux II optical microscope. The images were processed with the software Motic Images advanced 3.2 that allows image segmentation. The results were filtered to eliminate particles whose area was less than 20 pct of the average area of the total of the nodules. Finally, nodularity (n) is the shape factor that defines how close a circle is to the 2D image taken of each nodule and is determined by

$$n = \frac{4\pi A}{p^2}, \qquad [1]$$

where A and p stand for area and perimeter, respectively, of the 2D image for the analyzed nodule.

It is important to emphasize that by computing nodularity, the result is lower than that of an assessment by the traditional method of visual comparison, since these results are subjective and depend on the expertise of the evaluator. Figure 4 shows different nodules with their respective measured nodularity. For the first image, a nodule being evaluated traditionally would have a nodularity of 100 pct, but mathematically the value would be 85 pct. This is the reason why researchers have already determined how mathematical nodularity classifies cast irons. A cast iron is considered ductile when the nodularity varies between 100 pct $< n <$ 65 pct, is considered compact when it is between 65 pct $< n <$ 45 pct, and for values below that, the cast iron is considered gray iron.[25,26]

Temperature measurements taken for each melt are shown in Figure 5. A considerable loss of temperature ($\Delta T \approx 135$ K (135 °C)) was experienced from the moment the melt was taken out from the furnace until the final moment of inoculation. From the inoculation moment, temperature loss follows an almost linear behavior until reaching 1453 K (1180 °C) in minute 21. Additionally, it can be seen that even after 18 minutes of inoculation, the temperature of the melt had not passed the eutectic transformation temperature [1435 K (1162 °C)].

The microstructures obtained at each temperature point are shown in Figure 6 for the chilled samples, where there are austenite dendrites even at high temperatures[$T \sim 1463$ K (1190 °C)), confirming the multinodular theory proposed by Boeri.[5] As temperature decreased, an increase in the number of graphite nuclei growing in the shape of arms or rose petals was found. Therefore, the theory suggested by Zhou[11] is supported by the experimental results, where the final form of the nodule depends on the speed of encapsulation of graphite by the austenite.

III. NUMERICAL MODEL FOR SOLIDIFICATION

The solidification process was modeled by coupling two levels of analysis: On the one hand, there is the macroscopic level governed by the energy equation; on the other hand, the microscopic level which is governed by the microstructural model. Both problems are tightly coupled and, in general, present a high degree of nonlinearity. These problems are solved numerically through a time–space discretization in the context of finite differences and finite elements. Since the cooling process involves phase change in casting, heat transfer by conduction can be expressed using the heat equation[27]:

$$\rho c \dot{T} + \rho L \dot{f}_{pc} = \nabla \cdot (k \cdot \nabla T), \qquad [2]$$

where ρ is the density, c is the specific heat, k is the thermal conductivity, T is the temperature, L is the specific latent heat of phase change, and f_{pc} is the liquid volume fraction or the phase change function ($0 \le f_{pc} \le 1$).

During solidification, the rate of f_{pc} in each time step is given by the rates of the total fraction of austenite f_γ and precipitated graphite f_{gr} as

$$\dot{f}_{pc} = -(\dot{f}_\gamma + \dot{f}_{gr}). \qquad [3]$$

Table I. Average Chemical Composition

C	Si	Mn	S	P	Cr	Co	Mg	Fe	CE
3.765	1.908	0.287	0.009	0.014	0.031	0.015	0.017	bal.	4.40

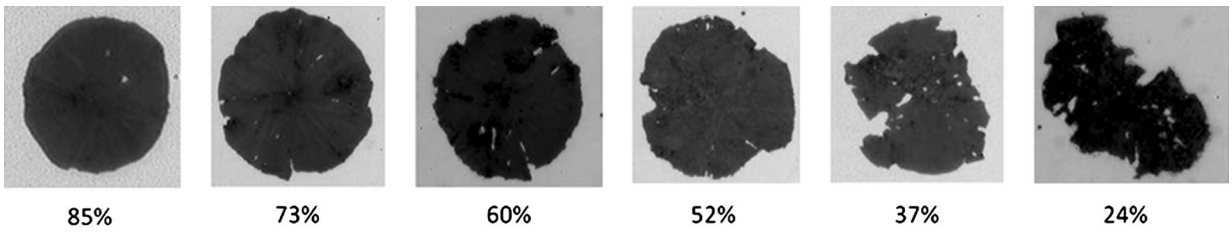

Fig. 4—Nodularity values calculated using mathematical models.

At the microstructural level, two eutectic models based on the multinodular theory were compared: (i) an existing model proposed by Boeri[5] that assumes a single carbon diffusion radius for graphite growth and (ii) a proposed model in which different carbon diffusion radii are used in order to evaluate nodularity.[28] In both cases, equiaxial solidification of a DI with eutectic composition was considered.

Regardless of the model used, the laws of nodule growth are based on chemical composition at interfaces. In addition, variations of the balance compositions due to silicon microsegregation are taken into account using the equilibrium diagrams by Heine *et al.*,[29] implemented for numerical simulations by Boeri.[5] With this in mind, the eutectic temperature can be obtained as

$$T_E = 11154.6 + 6.5\text{Si}. \quad [4]$$

The point of maximum solubility of carbon in austenite at eutectic temperature is given by

$$C_{TE} = 2.1 - 0.216\text{Si}, \quad [5]$$

and the carbon content at the eutectic temperature is described by

$$C_E = 4.26 - 0.317\text{Si}. \quad [6]$$

With the above equations, the percentages of carbon in the interface area can be calculated for each phase and temperature as

$$C_{\gamma}^{l} = \frac{1}{97.3}(1569 - T - 24.32\text{Si}), \quad [7]$$

$$C_{l}^{\gamma} = \frac{1}{177.9}(1528 - T - 32\text{Si}), \quad [8]$$

$$C_{gr}^{l} = \frac{1}{389.1}(T - 129.7\text{Si} + 503.2) \quad [9]$$

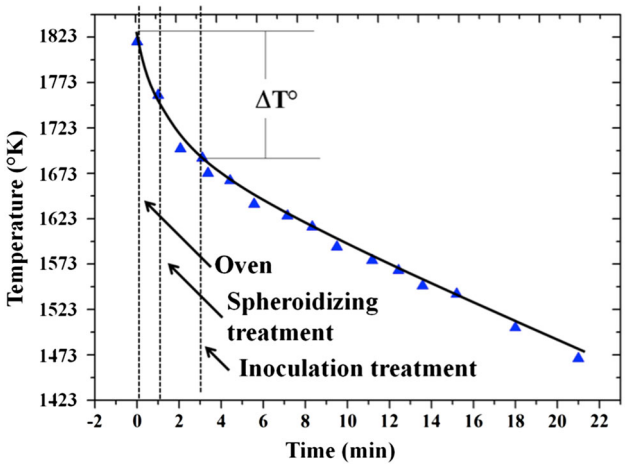

Fig. 5—Temperature change with time before pouring into the mold.

And, the solubility variation of carbon in austenite at the solid state is given by

$$C_{gr}^{\gamma} = \frac{(T - 1154.6 - 6.5\text{Si})(1.5 - 0.216\text{Si})}{(354.6 + 6.5\text{Si})} + 2.1 - 0.216\text{Si}, \quad [10]$$

where the coefficients $C^{l/\gamma}$, $C^{\gamma/l}$, $C^{l/gr}$, and $C^{\gamma/gr}$ are the equilibrium carbon concentrations at temperature T of liquid in contact with austenite, austenite in contact with liquid, liquid in contact with graphite, and austenite in contact with graphite, respectively. Si is the silicon concentration in the liquid, and it is calculated at each instant of the liquid–solid transformation using the Scheil's equation.[6]

A. *Graphite Nucleation*

To simulate graphite nucleation, a continuous exponential law was used in both models[13]:

$$\dot{N} = b\Delta T \exp\left(-\frac{c}{\Delta T}\right)(1 - f_s), \quad [11]$$

where b and c are parameters that remain constant for a given composition and liquid treatment, $\dot{N}$ is the density rate of graphite nodules, f_s is the solid fraction ($f_s = f_\gamma + f_{gr}$), and $\Delta T = T_E - T$ is the eutectic undercooling, with TE defined by Eq.[4].

When solidification begins, the release of latent heat is greater than the cooling rate; hence, temperature begins to rise. This process is known as recalescence (Figure 7).[6–8] Nucleation stops with recalescence due to the decrease of the undercooling needed by the inoculated graphite points in order to overcome the critical radius r^* and become a nodule.[8] Recalescence is an important phenomenon since according to it, two different behaviors have been postulated for graphite nucleation. Instant nucleation assumes that all possible graphite nuclei are created in one period of time before recalescence. On the other hand, in continuous nucleation, nodule nuclei can appear at different time periods during the cooling process due to the activation of small inoculated points that require an undercooling reached at the end of recalescence, allowing the presence of nodules of different sizes in a single casting piece.[30] It is important to evaluate these nucleation possibilities since a change in the nucleation process may affect nodularity as well as the cooling process.

B. *Growth of Graphite Nodules*

Boeri's[5] model (model B in the figures) proposes that graphite nucleates and grows, initially in contact with liquid, to be subsequently encapsulated by austenite. Growth in contact with liquid uses Zener's equation for a spherical isolated particle in a low supersaturated matrix, obtaining[5]

$$\dot{r}_l = \frac{1}{2r_l}\frac{C^{l/\gamma} - C^{l/gr}}{C^{gr} - C^{l/gr}}\frac{\rho^l}{\rho^{gr}}D_C^l, \quad [12]$$

where R_{gr} is the radii of the graphite sphere, $D_C^l$is the coefficient of carbon diffusion in liquid, while ρ_l and ρ_{gr} are the liquid and graphite densities, respectively.

Once the nodules reach 6 μm in diameter, Boeri's model assumes that they have already been surrounded by austenite. The choice of 6 μm as the upper diameter value for free growth of graphite in the liquid has been taken from the average of the experimental measurements of chilled samples during the solidification process, work done by Wetterfall *et al.*[12] From that moment on, it is assumed that graphite is reached by an austenite arm and gets surrounded by it. Growth begins to occur by diffusion of carbon from the liquid to the graphite through the austenite. And, so the growth law becomes

$$\dot{r}_\gamma = \frac{1.911}{r_\gamma}\left(\frac{C^{\gamma/l} - C^{\gamma/gr}}{1 - C^{\gamma/gr}}\right)\frac{\rho^\gamma}{\rho^{gr}}\, D_C^\gamma\, (1 - f_s)^{2/3}. \qquad [13]$$

With Boeri's model, the final nodule has a round shape, since it is completely surrounded by either liquid or austenite throughout the solidification process. Taking into account that it is an alloy and not a pure metal, the phase change process is not immediate, *e.g.*, between the transformation from liquid to solid phase, there is a mushy phase in which the nodules are not perfectly covered by a single phase. This generates different

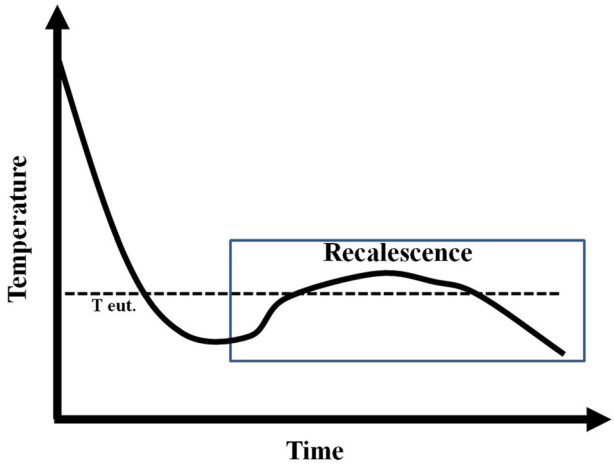

Fig. 7—Recalescence experienced during DI solidification process.

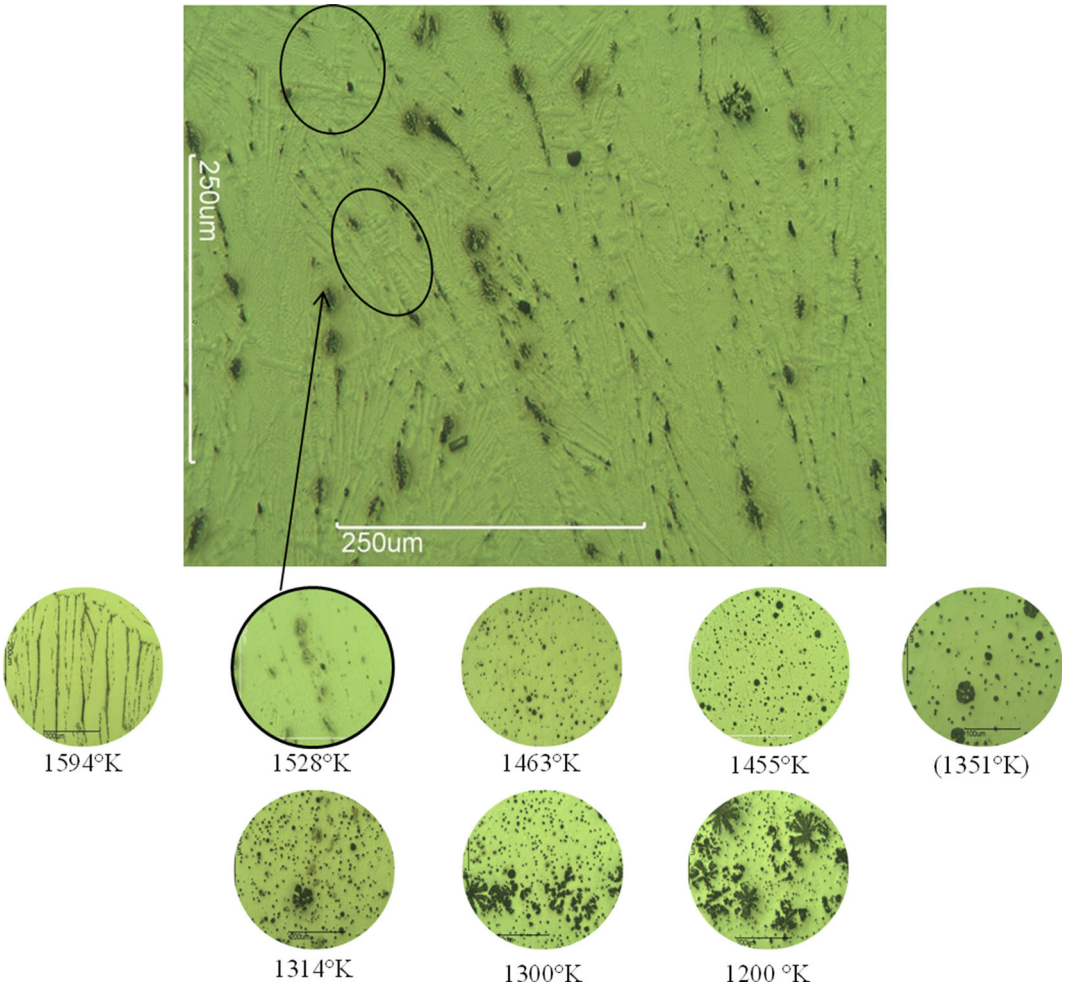

Fig. 6—Microstructure at different steps during the solidification process for the chilled samples. Temperatures at which each microstructure was evaluated are indicated below each picture.

growth radii according to the coupling process between austenite and graphite, as schematically shown in Figure 8.

Despite the fact that different researchers have found experimental evidence of the aforementioned,[9,11,12] few have ventured to set a transition limit to define one growth law or another. This is why a majority of the existing numerical models define an experimental constant to define the change in growth law. Here, a model is proposed that takes into account that solidification is not an immediate phase change process, identifying intervals based on the percentage of solid phase for each growth law (model N in the Figures). As schematically shown in Figure 9, different ranges of transition were studied, and based on the experimental data found for

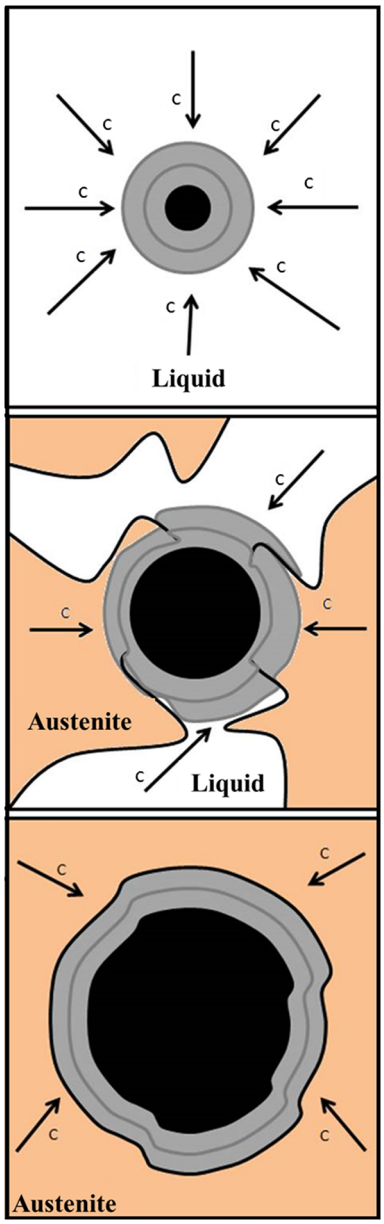

Fig. 8—Nodule growth according to the surrounding phase: (*a*) liquid; (*b*) austenite, and liquid; and (*c*) austenite.

nodularity and nodule count, the following intervals were defined (complete analysis of different solidification intervals can be found in Reference 28): at the beginning, between $0 < f_s < 0.3$, each nodule is surrounded by liquid, therefore Eq.[12] is used. Then, as the solid fraction increases ($0.3 < f_s < 0.8$), nodules are surrounded by austenite and liquid. Hence, nodules grow with two different laws; one half of the nodule grows in contact with liquid (Eq.[12]) and the other half grows in contact with austenite (Eq.[13]). Finally, when the casting is almost solidified ($0.8 < f_s < 1$), the nodule finishes its growth in each radius in contact with austenite (Eq.[13]). Using two laws of growth in a single interval generates a difference of radii in the nodule, which induces a change of the spherical geometry and allows variations of nodularity, as seen experimentally.

Nodularity is defined by Eq.[1], where the area is expressed by

$$A = \frac{\pi}{2}\left(r_1^2 + r_\gamma^2\right), \qquad [14]$$

and the perimeter is calculated as

$$p = \pi\left(r_1 + r_\gamma\right) + 2\left(r_1 - r_\gamma\right). \qquad [15]$$

Finally, mean nodularity is calculated as

$$\bar{n} = \frac{\sum_1^i N_i n_i}{\sum_1^i N_i}, \qquad [16]$$

where i is the number of nucleated groups during solidification and N is the number of nodules in each family.

C. *Graphite and Austenite Fractions*

In order to implement the proposed nodule growth model, it was necessary to define the graphite fraction present at each time increment. Each nodule has different radii, giving a graphite fraction defined as

$$f_{gr} = \sum_1^k \frac{2}{3}\pi N_k\left(r_l^3 + r_\gamma^3\right), \qquad [17]$$

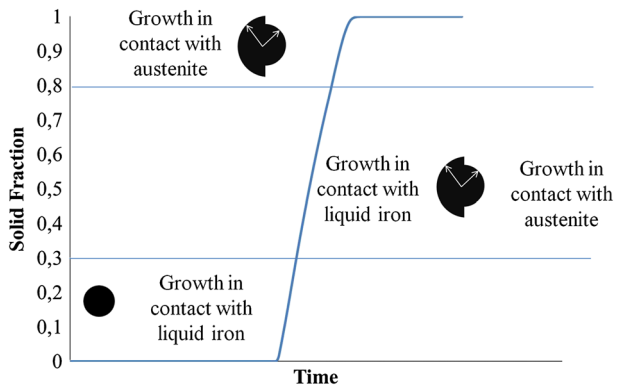

Fig. 9—Schematic diagram of the proposed nodule growth scheme.

where r_l and r_γ are the radii created in contact with liquid and austenite, respectively. It should be noted that Boeri's model also uses Eq.[17] assuming that $r_l = r_\gamma$.

A constant relationship between the amount of austenite and graphite is considered for austenite growth. This relationship is given by the lever rule applied to the eutectic equilibrium:

$$\text{REAG(pct)} = \frac{100 - C_E}{C_E - C_{TE}}, \quad [18]$$

Lastly, the austenite fraction is calculated as a function of graphite fraction as

$$f_\gamma = f_{gr}(\text{REAG}), \quad [19]$$

and the solid fraction can be calculated as

$$f_s = f_{gr}(1 + \text{REAG}). \quad [20]$$

IV. COMPARISON BETWEEN EXPERIMENTAL AND COMPUTATIONAL RESULTS

The experimental results from the 30-mm-thick specimens were selected to carry out detailed comparisons with the numerical results of the computational formulations for temperature and metallographic measurements of nodule count and nodularity. Computations were performed using VULCAN, a code programed in Fortran.[31] One casting element was used, and a constant thermal flux extraction was set with unidirectional flow. A 1D simulation can demonstrate the solidification process in the same way as a 3D simulation would, since temperature does not change in the microstructural variables if any type of gradient is eliminated. Therefore, transversal temperature changes are not experienced (similar to axisymmetric analysis in solid mechanics). Accordingly, the energy equation is considered 1D, but the microstructural model is still 3D.

The parameters and coefficients used for the numerical simulations are listed in Table II. A time-dependent heat transfer coefficient has been considered here in order to account for the solidification of the melt inside the ladle due to the casting process. In this way, the melt passes through three stages during its solidification: (i) solidification in the ladle, (ii) pouring, and (iii) solidification inside the mold. Each of these stages involves a change in the heat extraction reflected in the heat transfer coefficient h. Based on experimental results, h was set as (i) 0.95 W/m^{2}K for solidification in the ladle, (ii) 35 W/m^{2}K for pouring, and (ii) 9.35 W/m^{2}K for solidification inside the sand mold.

The constants b and c in Eq.[11] reflect the quality of the chemical treatment and the materials used. These were calculated with the help of macrostructural simulation and the experimental values of temperature loss and morphological characteristic. For instant nucleation, values of $b = 6 \times 10^{22}$ nuclei/(m^3 K s) and $c = 773$ K (500 °C) were used. For continuous nucleation, values of $b = 4 \times 10^{13}$ nuclei/(m^3 K s) and $c = 613$ K (340 °C) were used.

Figure 10 shows the cooling curves predicted by the studied models. As there are different rates for latent heat release due to the change in the growth law, different plateaus appear for the cooling curves for the proposed model (model N) in comparison with the cooling curve predicted by Boeri's model (model B). With the continuous nucleation model, there is a greater release of latent heat during solidification reflected in an increase of temperature during recalescence. In addition, phase transformation starts earlier when using the proposed nodularity model with instant nucleation due to a higher undercooling as a consequence of the nucleation of all nodules in a single time step.

The evolution of the liquid fraction depends on the release of latent heat conditions during solidification. Figure 11 shows the evolution of the liquid fraction for each of the models used. The changes in the cooling rate with nucleation models can be appreciated in the solid fractions defined as a growth law changing point (*i.e.*, 0.3 and 0.8 of solid fraction). This confirms that the

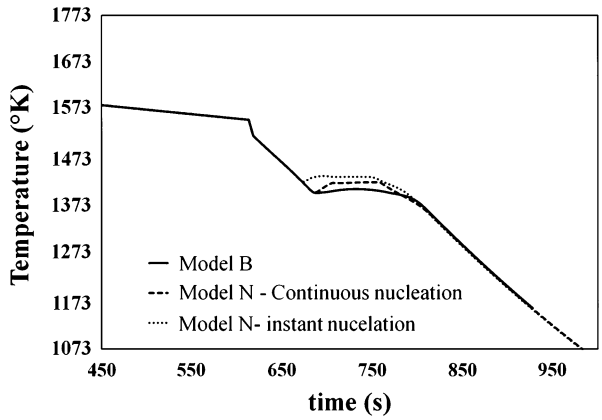

Fig. 10—Predicted cooling curves.

Table II. Temperature-Dependent Properties of Ductile Iron

Property	Value	Temperature [K (°C)]
Density (kg/m3)	7000	—
Specific heat (J/kg K)	550	273 (0)
	704,182	1403 (1130)
	915	1473 (1200)
	915	1573 (1300)
Thermal conductivity (W/K m)	42	—
Solidification temperature [K (°C)]		1428 (1155)

change in release of latent heat is due to the chosen growth law. The most pronounced change of slope appeared for the continuous nucleation model, achieving higher latent heat release at the beginning of the transformation (growth in the liquid) than at the end of this process (growth in austenite).

Figure 12 shows the evolution of nodules' count along the solidification process for continuous and instant nucleation. As mentioned previously, in instant nucleation, all possible nucleation points are generated on a time increment (Δt) before reaching recalescence. After that, nodule count remains constant during the rest of the solidification process. In comparison, the results for continuous nucleation have an initial increase of nucleation points before recalescence, and once recalescence has finished, the nucleation process restarts exponentially (see Eq.[11]) until the solid fraction does not allow the generation of new graphite points. Additionally, the volumetric nodule count (graphite nodules/mm^3) is higher for continuous than for instant nucleation. This behavior is explained by the longer time period required for eutectic transformation in the instant nucleation model, as a consequence of the lower number of nodules that can nucleate. Finally, regardless of the nucleation model used, there is a change in the final nodule count with different pouring temperatures, which suggests a possible reproduction of the experimental results for the morphological characteristics that will be shown below.

Experimental and numerical results for the change of nodule count after solidification with pouring temperature are shown in Figure 13. Since the numerical results are given as nodules per volume, it was necessary to convert this result to nodules per area. The following formula was used to change from volume to area nodule count[17]:

$$N_{2D} = N_{3D}\frac{4r}{3}, \qquad [21]$$

where r are the average radii.

Experimental results have a changing behavior according to the pouring temperature that cannot be explained by a poor inoculation treatment, since even with the lowest pouring temperature [~1473 K (~1200 °C)], there is a higher nodule count in comparison with the results from the first pouring temperature [1673 K (1400 °C)]. Boeri's model fails to predict this behavior, showing constant nodule count values through the range of pouring temperatures. Unlike the results obtained with Boeri's model, the nucleation model presents variability of the nodule count with pouring temperature. Even so, the results show a behavior opposite to the one found experimentally; that is, when there is an experimental increase in the nodule count, a decrease in the numerical result was found. The highest degree of agreement with the experimental results was reached using the instant nucleation model.

This kind of behavior is explained by Eq.[11], where nucleation is ruled by the eutectic undercooling and does not include an initial undercooling due to the pouring temperature, which is important because it determines the nodule radii. According to previous studies, it is known that there is an inverse relationship between the radii of the nodules and the amount of nodules in a sample, *i.e.*, higher nodule count comes with smaller nodules.[21,32] This is a well-studied behavior found where there are changes in the cooling rate. It is well known that during solidification of nodular irons, the heat extraction rate is important.[18,29,32] A higher cooling rate gives higher nodule count with smaller radii than the ones that would be found with low cooling rates. This indicates that the change in the pouring temperature induces a source of heat extraction that is not considered in the present models, and is important since it gives the necessary driving force for the nucleation of smaller nodules.

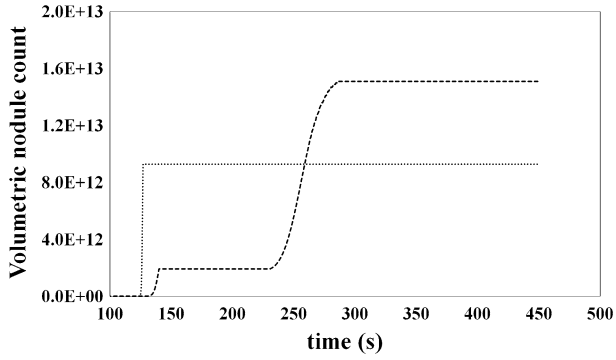

Fig. 12—Numerical results for nodule count evolution using the proposed nodularity model for continuous and instant nucleation. Similar curves were found for different pouring times.

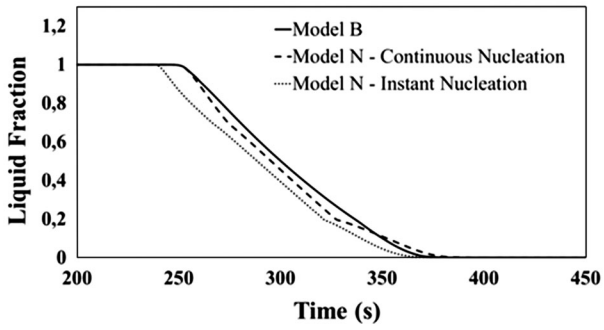

Fig. 11—Predicted results for evolution of the liquid–solid fraction through solidification with models N and B.

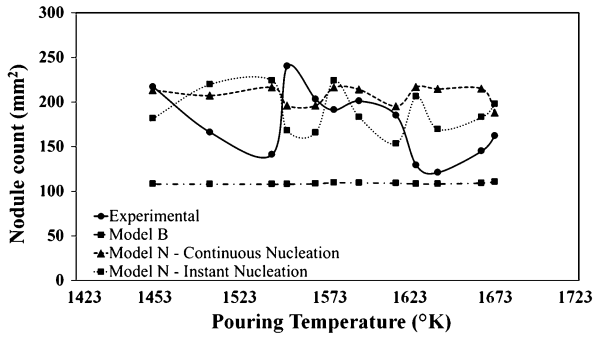

Fig. 13—Nodule count *vs* pouring temperature. Experimental and numerical results are shown.

The relationship between nodule radius and count is shown in Figure 14(a), including experimental and numerical results. When comparing the models for nucleation, on average, nodules with greater radii are predicted using instant nucleation. This is due to a longer period of time for carbon diffusion than the one experienced with continuous nucleation. In spite of perceiving slight changes in the average radii, Boeri's model is unable to perceive any relationship between nodule radii and count. In comparison with the proposed nodularity model, the continuous nucleation model reaches an incremental behavior, which is the opposite for the experimental behavior. Although the results obtained with instant nucleation present a variation in the nodule count, the mean radius remains constant, which is different from the behavior found following continuous nucleation. The real variation of radii with nodule count for instant nucleation can be observed with the ratio of nodule growth (r_γ/r_1), since a change in the average radii is caused by a difference in the ratio growth at the end of the solidification. The relationship between nodule count and ratio of nodule growth for instant nucleation can be found in Figure 14(b), where a trend similar to that found with continuous nucleation is generated (Figure 14(a)). This behavior verifies that nucleation models are able to predict a similar relationship to the one found experimentally, but in order to get the same trend between nodule ratio and average count of nodules, it is necessary to account for an initial undercooling due to pouring, as a variable in the nucleation model.

In Figure 13, it is seen that with the proposed nodularity model and instant nucleation there is a greater variation of nodule count than with continuous nucleation. To explain this difference, Figure 15 shows how the initial undercooling is related to nodule count. It can be seen that for the two models, there is a negative trend between the initial undercooling and the nodule count. This negative relationship becomes more evident with instant nucleation since in this case the initial undercooling is the one that provides the necessary energy for the creation of all of the nucleation points. In comparison to continuous nucleation, the initial undercooling is only important for the initially nucleated nodule before recalescence, and as seen in Figure 12, a majority of the nodules are created after recalescence.

Figure 16 shows the evolution of nodularity through the solidification process for both nucleation models. It can be seen that while the nodules are surrounded by liquid ($0 < f_s < 0.3$), they follow one growth law, achieving a nodularity equal to one. Then, nodularity drops as the mushy zone is approached ($0.3 < f_s < 0.8$),

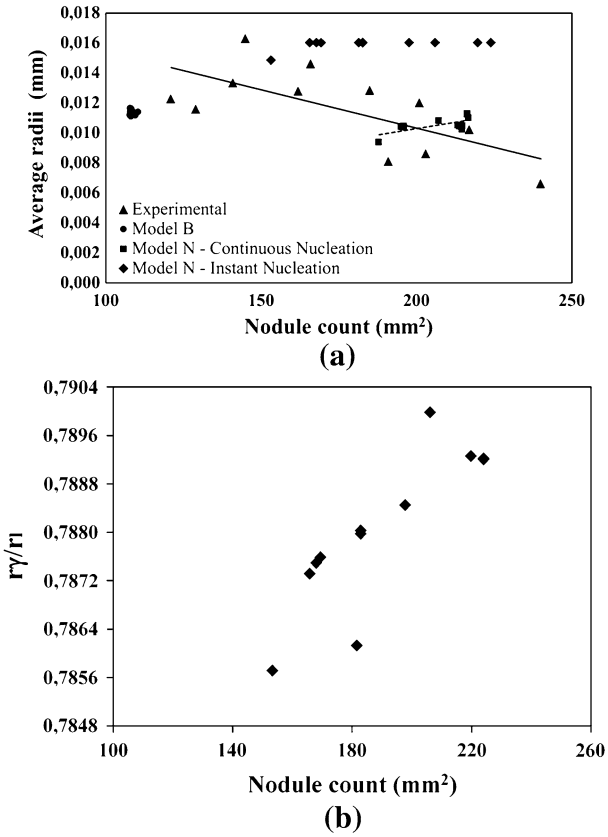

Fig. 14—(*a*) Relationship between average radii and nodule count for experimental and numerical results; and (*b*) Numerical results for the growth ratio *vs* nodule count for instant nucleation using the proposed nodularity model.

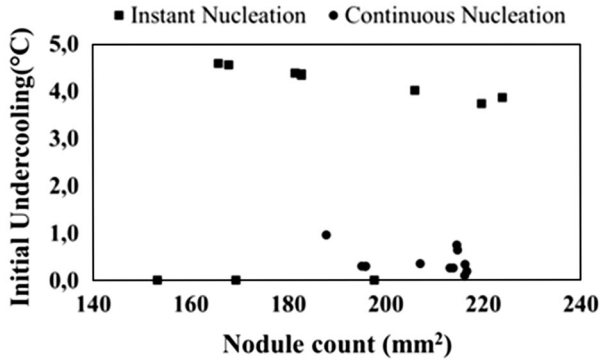

Fig. 15—Numerical relationship between the Initial Undercooling *vs* nodule count found using the proposed nodularity model and the nucleation models.

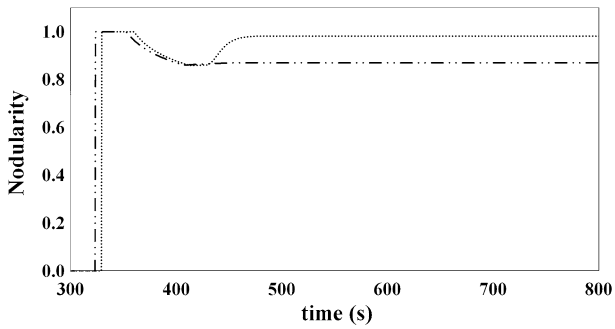

Fig. 16—Numerical results for nodularity evolution through time found using the proposed nodularity model for continuous and instant nucleation. Dotted line represents continuous nucleation ($tv = 3$); Dashed line represents instant nucleation ($tv = 3$).

due to the growth of the nodules with two different radii. As the nodules are completely surrounded by austenite ($0.8 < f_s < 1$), there is a change in the nodularity behavior depending on the nucleation model used. For instant nucleation, there is a slight increase in nodularity up to a value close to 86 pct. In comparison, for continuous nucleation, nodularity increases up to a value close to the perfect nodularity. The apparent regain of nodularity is due to the amount of nodules that nucleate after recalescence. When recalescence stops, most of the metal is solidified ($0.8 < f_s < 1$); therefore, the new nucleated nodules grow entirely surrounded by austenite. Since most of the nodules in continuous nucleation are created after recalescence (they grow with a circular shape), the average value of nodularity increases.

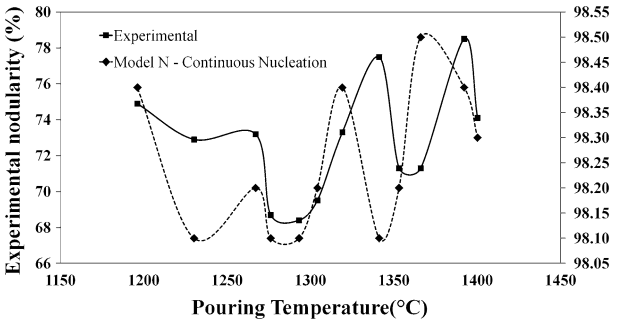

Fig. 17—Nodularity *vs* pouring temperature. Experimental and numerical results for continuous nucleation are shown.

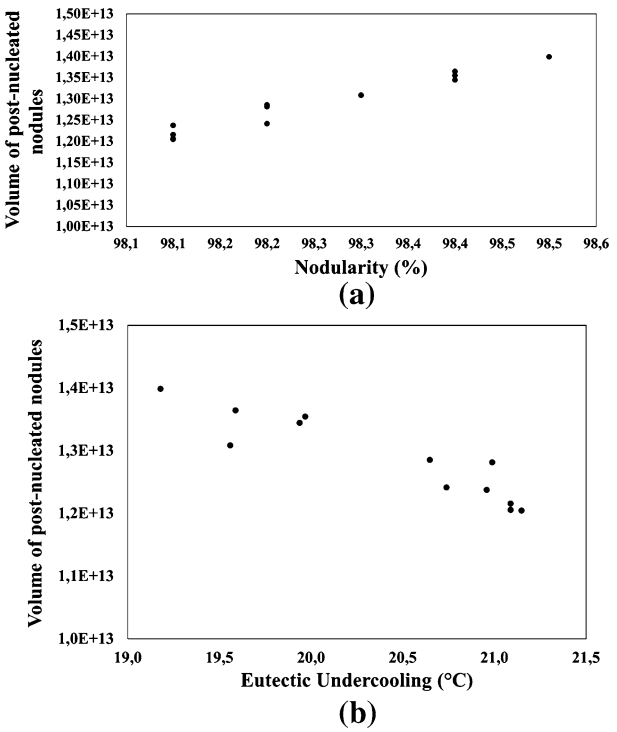

Fig. 18—Post-nucleated nodules *vs* (*a*) nodularity; and (*b*) eutectic undercooling.

Figure 17 shows how nodularity changed experimentally and it is compared with the values calculated with the proposed nodularity model and continuous nucleation. In spite of not achieving the exact experimental values, it can be seen that the numerical results follow a similar tendency. Nodularity found with instant nucleation is not shown since it presents no variation with different pouring temperatures.

Nodularity presents changes with continuous nucleation thanks to the number of nodules that nucleate after recalescence. This can be seen in Figure 18(a) where a linear relationship between nodularity and numerical post-nucleation nodules is found. As explained before, the amount of nodules that can nucleate after recalescence depends on the eutectic undercooling. Figure 18(b) shows the variation of the post-nucleated nodules with the eutectic undercooling found numerically, confirming that the eutectic undercooling affects nodularity.

V. CONCLUSIONS

During solidification of ductile irons, there are microstructural changes that initially depend on chemical treatments such as nodulization and inoculation. However, it was experimentally found that there are changes in both nodule count and nodularity depending on pouring temperature. The existing microstructural models for nodular iron solidification do not predict these changes as they only predict nucleation points according to eutectic undercooling. In this work, a new model was proposed for the microstructural evaluation of nodularity during solidification. The growth process of the nodules was based on different laws for carbon diffusion according to the solid fraction. The new microstructural model was evaluated under two nucleation schemes that differ on how graphite growth points are generated: instant and continuous nucleation. Thanks to the simulations performed with instant nucleation, the experimental variation of nodule count with pouring temperature was explained. Initial undercooling is an important driving force for the nucleation of graphite that is strongly influenced by pouring temperature, and it must be considered in addition to the eutectic undercooling. Moreover, the new model can predict the experimental behavior found for average nodularity. It was also found that nodularity of a sample depends on the number of nucleation points generated after recalescence, which change with the eutectic undercooling due to changes in pouring temperature.

ACKNOWLEDGMENTS

The authors would like to express their gratitude to the foundry Furima S.A.S, Medellín, Colombia, for providing the materials used in this study. It is also important to acknowledge the economic support for this study provided by the Administrative Department of Science, Technology and Innovation, Colciencias (Colombia), Contract No. 525-09. Finally, the authors

gratefully acknowledge the financial support provided by FONDECYT (Project No. 1130404).

REFERENCES

1. S. Murcia, M. Paniagua, and E. Ossa: *Mater. Sci. Eng. A*, 2013, vol. 566 (20), pp. 8–15.
2. K. Kocatepe, M. Cerah, and M. Erdogan: *J. Mater. Process. Technol.*, 2006, vol. 178, pp. 44–51.
3. M. Hafiz: *J. Mater. Sci.*, 2001, vol. 36, pp. 1293–300.
4. A. Basso and J. Sikora: *Int. J. Metalcast.*, 2012, vol. 6, pp. 7–14.
5. R.E. Boeri: Ph.D. Thesis, University of British Columbia, 1989.
6. P.M. Dardati: Doctoral Thesis, Universidad Nacional de Córdoba, 2005.
7. G. Rivera, R. Boeri, and J. Sikora: *Mater. Sci. Technol.*, 2002, vol. 18, pp. 691–97.
8. E. Fra and H. López: *Int. J. Metalcast.*, 2010, vol. 4, pp. 35–61.
9. D.M. Stefanescu: *Science and Engineering of Casting Solidification*, Springer, New York, 2008.
10. C. Arturo: *Análisis Experimental y Numérico de la solidificación de las Fundiciones Nodulares*, vol Ingeniero Civil, Universidad de Chile, Santiago, 2005.
11. J. Zhou: *China Foundry*, 2011, vol. 8, pp. 447–62.
12. S.E. Wetterfall, H. Fredriksson, and M. Hillert: *J. Iron Steel Inst.*, 1972, vol. 210, pp. 323–33.
13. K.C. Su, I. Ohnaka, I. Yamauchi, and T. Fukusako: *MRS Proc.*, Cambridge University Press, vol. 34, 1984.
14. F. Edward: *MRS Proc.*, Cambridge Univ Press, vol 34, 1984.
15. D. Stefanescu and C. Kanetkar: *Computer Simulation of Microstructural Evolution*, The Metallurgical Society, Warrendale, 1985, pp. 171–88.
16. D. Stefanescu and D. Bandyopadhyay: in *Physical Metallurgy of Cast Iron IV*, MRS, Pittsburg, 1989, pp. 15–26.
17. A. Chiarella: *Análisis Experimental y Numérico de la solidificación de las Fundiciones Nodulares*, vol Ingeniero Civil, Universidad de Chile, Santiago, 2005.
18. A.F.M.S.S. Inc: *AFS Ductile Iron Handbook*, AFS, Des Plaines, 1993.
19. H. Fredriksson and I.L. Svensson: *MRS Proc.*, Cambridge Univ Press, vol. 34, 1984.
20. S. Chang, D. Shangguan, and D. Stefanescu: *Ninety-Fifth Annual Meeting American Foundrymen's Society*, 1991, pp. 531–41.
21. S.C. Murcia: *Estudio del efecto de las variables de proceso sobre la calidad final en fundiciones de hierro nodular*, vol Production Engineer, Eafit University, 2010.
22. A. Kim, S.L. Cockcroft, and A.M. Omrana: *J. Alloy. Compd.*, 2009, vol. 476, pp. 728–32.
23. R.B. Gundlach: *Nodularity, its Measurement, and its Correlation with the Mechanical Properties of Ductile Iron*, Stork Climax Research Services, Michigan, 2006.
24. ASTM E3-01: *Standard Practice for Preparation of Metallographic Specimens*, ASTM International, Philadelphia, 2001, 12pp.
25. B. Imasogie and U. Wendt: *J Miner. Mater. Charact. Eng*, 2004, vol. 3, pp. 1–12.
26. A. SheikhAbdolhossein and M. Nili-Ahmadabadi: *Int. J. Cast Met. Res.*, 2005, vol. 18, pp. 295–300.
27. D.J. Celentano, S.O. Martínez, and E.O.I. de Navarra: *Un Modelo Termomecánico para Problemas de Solidificación de Metales*, Universitat Politècnica de Catalunya, Barcelona, 1994.
28. S.C. Murcia: M.Sc. Thesis, Universidad Eafit, 2012.
29. R.W. Heine, C.R. Loper, and P.C. Rosenthal: *Principles of Metal Casting*, McGraw-Hill, Tokyo, 2001.
30. W. Kapturkiewicz, A.A. Burbelko, E. Fraś, M. Górny, and D. Gurgul: *J Achiev. Mater Manuf. Eng.*, 2010, vol. 43, pp. 310–23.
31. D. Celentano: VULCAN: Coupled Thermomecanical Finite Element Analysis for Solidification Problems, User's and Verification Manuals, 2004.
32. S. Bockus and G. Zaldarys: *Metalurgija*, 2009, vol. 48, p. 19.